A complete structural model and kinematic history for distributed deformation in the Wharton Basin

Duncan E. Stevens[a,*], Lisa C. McNeill[a], Timothy J. Henstock[a], Matthias Delescluse[b], Nicolas Chamot-Rooke[b], Jonathan M. Bull[a],

[a]Ocean and Earth Science, National Oceanography Centre Southampton, University of Southampton, Southampton, S014 3ZH, United Kingdom

[b]ENS Laboratoire de Géologie, CNRS UMR8538, PSL Research University, Paris, France

*Corresponding author: des1g12@soton.ac.uk

A B S T R A C T

The equatorial eastern Indian Ocean hosts a diffuse plate plate boundary, where widespread deformation accommodates the relative motion between the Indian, Australian and Capricorn sub-plates. We integrate IODP Expedition 362 borehole data, which for the first time provides an accurate, ground-truthed chronostratigraphy of the sedimentary sequence east of the Ninety East Ridge (NER), with 2D seismic reflection profiles and multibeam bathymetry to assess the styles of faulting between the NER and the Sunda subduction zone, timing of activity and comparison with physical and rheological properties. We identify four distinct fault sets east of the NER in the northern Wharton Basin. N-S (350-010°) orientated faults, associated with the N-S fracture zones formed at the now extinct Wharton spreading centre, are still active and have been continuously active since at least 10 Ma. NNE- and WNW-trending fault fabrics develop between the fracture zones. The orientations and likely sense of displacement on these three sets of faults defines a Riedel shear system responding to ~NNE-SSW left-lateral strike-slip activity at depth, demonstrated by the recent 2012 great intraplate earthquakes. We also find evidence of ~NE-SW reverse faults, similar in style to E-W reverse faults observed west of the NER, where reverse faulting is more dominant. We show that the

activity of this strike-slip system increased ca. 7-9 Ma, contemporaneous with reverse faulting and intraplate deformation west of the NER.

Keywords: Intraplate deformation; Indian Ocean; Diffuse plate boundary; IODP.

1 Introduction

The oceanic lithosphere of the equatorial Indian Ocean hosts a 3000 km wide (West to East) zone of complex deformation representing a diffuse plate boundary between the Indian, Capricorn and Australian plates (DeMets et al., 1990; Stein and Okal, 1978; Sykes, 1970; Wiens et al., 1986). The relative motion between the three plates, and the transfer of stress from plate boundaries surrounding the Indian Ocean, results in a variation in sense and style of deformation across the diffuse plate boundary (Fig. 1) (DeMets et al., 1990; Gordon et al., 1998; Wiens et al., 1986). The Ninetyeast Ridge (NER), a north-south aseismic ridge, that stretches from ~34°S to ~10°N (~90°E), seems to play a role in the west to east variation in deformation. West of the NER, deformation is characterised by crustal shortening (Bergman and Solomon, 1985; Bull, 1990; Stein and Okal, 1978; Wiens et al., 1986), whereas in the equatorial Indian Ocean, at the northern end of the NER and east of the NER (the northern Wharton Basin, Fig. 1), primarily left-lateral strike-slip motion dominates (Deplus, 2001; Deplus et al., 1998; Sager et al., 2013). The change in deformation is likely due to the increased proximity and influence of the Sunda subduction zone.

The northern Wharton basin (north of 10°S) includes sediments of the Nicobar Fan, part of the Bengal-Nicobar Fan system (McNeill et al., 2017a). The complete sedimentary section was sampled by International Ocean Discovery Program (IODP) Expedition 362 to basement at 1415 m below seafloor (mbsf) (McNeill et al., 2017b). Fan sediments are dominated by siliclastic sediment gravity-flow deposits (e.g., turbidity currents and debris flows), that range from clay to silty clay to fine-grained sand. These are underlain by pelagic and tuffaceous sediments overlying ocean basement (McNeill et al., 2017b). Sediments are mostly unlithified, with lithified sediments only encountered in the deepest intervals.

Compressional deformation west of the NER, between 6°N and ~8°S, is well documented (e.g. Bergman and Solomon, 1985; Bull et al., 2010; Bull and Scrutton, 1990, 1992; Chamot-Rooke, 1993; Krishna et al., 2001, 2009; Stein et al., 1989; Stein and Weissel, 1990; Stein and Okal, 1978) by the integration of seismic reflection data with information from ocean drilling sites (ODP Leg 116, DSDP 215, 218). Deformation takes place along E-W trending reverse faults, i.e. ~N-S compression, interpreted as reactivating the original ridge-parallel spreading fabric due to stress transfer from the N-S continental collision between India and Eurasia (e.g., Bull and Scrutton, 1992, 1990; Chamot-Rooke, 1993). Fault reactivation here started at ~14-15.5 Ma (Krishna et al., 2009), with suggestions of increased activity at ~7-8, 4-5 and 0.8 Ma (e.g. Bull et al., 2010; Krishna et al., 2001). Bull et al. (2010) showed that increased compressional deformation at ~7-8 Ma (e.g. Krishna et al., 2009) coincides with the acceleration of Indian-Capricorn rotation and relative convergence from plate motion models (DeMets et al., 2010, 2005). Many have suggested that the timing of pulses in distal fault activity are related to uplift of the Himalayas and Tibetan Plateau (Bull et al., 2010; Gordon, 2009; Merkouriev and DeMets, 2006; Molnar and Stock, 2009), buckling the Indo-Australian lithosphere (Copley et al., 2010; Weissel et al., 1980). However, studies of the Himalayas and Tibet have generated a range of timings for activity and accelerated deformation over the last 20 Ma (e.g. Clift et al., 2008; Molnar et al., 1993; Molnar and Stock, 2009), therefore correlating discrete collisional/uplift episodes with phases of distal compressional deformation is challenging. Alternatively, Iaffaldano et al., 2018 have suggested that an acceleration in compressional deformation at 7-8 Ma within the Indo-Australian plate may be linked to increased asthenospheric flow resulting from the re-emergence of volcanism along the Rodrigues Ridge at 11 Ma.

Until now the timing of intraplate deformation in the Indo-Australian plate has not been well-constrained east of the NER. There are fewer studies of deformation (e.g. Deplus et al., 1998; Geersen et al., 2015; Singh et al., 2017; Hananto et al., 2018), and until recently there has been no direct age control. Seismicity is generally characterised by left-lateral strike-slip motion on reactivated N-S trending fracture zones that offset the E-W trending Wharton Ridge, a fossil spreading centre (Deplus, 2001; Deplus et al., 1998). Spreading at the Wharton Ridge was active at least as early as 84 Ma, separating India from Australia, but ceased around 42 Ma (along with related transform fault/fracture zone activity), with the Indian and Australian plates becoming a single plate (Liu et al., 1983). The same tectonic driving mechanism responsible for compressional deformation west of the NER may also have reactivated the Wharton Ridge fracture zones but the reactivation timing of the latter is unclear. The difference in deformation style on either side of the NER may be due to variation in the stress field within the Indo-Australian plate with the Sunda subduction zone causing the principal stress in the Wharton basin to be NNW-SSE, compared to N-S west of the NER (Gordon and Houseman, 2015).

In April 2012, the largest and most complex strike-slip earthquakes ever recorded ruptured a set of WNW-ESE and NNE-SSW fault planes oblique to the N-S fracture zones. The initial mainshock ruptured along a WNW trending fault with a centroid depth of ~30 km with a M_w of 8.6, that initiated multiple ruptures to the north and south on NNE trending faults at similar depths, this was then followed by another M_w 8.2 earthquake that ruptured a WNW trending fault ~180 km to the south (Fig.1; e.g. Duputel et al., 2012; Hill et al., 2015; Wei et al., 2013). Recent studies have identified faults/lineations from bathymetry data with similar orientation to faults modelled to have ruptured (e.g. Geersen et al., 2015; Hananto et al., 2018; Singh et al., 2017). The various orientations observed have been interpreted as a Riedel shear system related to the reactivated N-S fracture zones (Geersen et al., 2015; Hananto et al., 2018). Geersen et al. (2015) suggested these Riedel shear fabrics developed around 20 Ma, with fracture zones reactivated since 40 Ma. However, these timings were based on pre-drilling chronostratigraphic estimates.

Data from IODP Expedition 362 boreholes provides the first ever core-stratigraphic ages for the sedimentary sequence east of the NER (McNeill et al., 2017b). These data indicate that the chronostratigraphy of the sedimentary sequence is significantly different to that previously assumed. Based on this new information, we update here the activity timings of all types of fault in the northern Wharton Basin, east of the NER. In addition, we have conducted a thorough integration between the seismic and bathymetry data in the study area, to derive fault orientations and fault types. Together, these new integrated data enable us to perform a more complete fault analysis. We also directly compare our results, east of the NER, with previous studies west of the NER, for the first time with chronostratigraphy in both locations, to correlate and examine existing discrepancies between deformation events and fault activity timing across the eastern Indian Ocean and discuss potential deformation forcing mechanisms. We also use the IODP results to test relationships between faulting and the lithological and physical properties of the oceanic plate sediments.

2 Methods

2.1 MCS Data and Interpretation

We have re-interpreted multichannel seismic reflection (MCS) data from the northern Wharton Basin (e.g. Fig. 2) (building on Dean et al., 2010; Geersen et al., 2015; Geersen et al., 2013; McNeill et al., 2017a). The seismic data are two composite SW-NE profiles A(BGR06 101-102) and B (BGR06 103-104-105) from Gaedicke (2007; Cruise SO186 on FS Sonne) which extend from the NER to the Sunda subduction zone at North Sumatra (Fig. 1), and NW-SE profile C (MD116-ANDAMAN84) from Chamot-Rooke (2000; Cruise MD116 on the R/V Marion Dufresne). The seismic data have a vertical resolution of ~10-15 m. We interpret all faults with maximum vertical offsets > 10 ms of two-way-travel-time (TWT) (approx. 10 m), including blind faults (some obvious blind faults were interpreted that have less than <10 ms vertical separation). We interpret and use roughly evenly spaced seismic horizons R1-R14 that can be continuously correlated. Some of these reflectors are equivalent to those of Geersen et al. (2015), while R11 corresponds to the 'High-Amplitude-Negative-Polarity' (HANP) pre-décollement reflector of Dean et al. (2010). We locally interpret additional reflectors to allow detailed analysis of selected faults.

2.2 Integration with IODP Expedition 362 borehole data

All three seismic profiles intersect IODP Expedition 362 borehole sites U1480 and U1481 where sonic log and core-log seismic integration (McNeill et al., 2017b) allow us to determine the depth intervals of reflectors R3 to R12, and R14 and correlate borehole data to the seismic stratigraphy. Age control is based primarily on calcareous nannofossils, and we note that the age markers are approximate (see Fig. 3; McNeill et al., 2017a, 2017b). The section is dominated by Nicobar Fan sedimentation since 9-10 Ma in contrast to the older pre-drilling predicted ages used by Geersen et al., (2015). We also compare fault displacement with other parameters in the IODP boreholes, including lithology, physical properties (e.g., porosity, velocity), and fracture intensity.

2.3 Multibeam processing and interpretation

We reprocessed a subset of the multibeam bathymetry data from cruise SO186 collected using the SIMRAD EM120 Multibeam System. We applied an updated and improved sound velocity profile correction, a ship roll correction and removed spikes from individual pings, to improve the signal to noise ratio of the true seafloor topography. We then re-interpreted this data and re-interpreted multibeam data from cruise MD116.

2.4 Vertical offset measurements

We measured the vertical offset/throws (hereafter referred to as displacements) for reflectors R2 to R12 across all interpreted faults on the NE-SW seismic profiles. We developed a semi-automated method which relies on the precise and consistent interpretation of the reflectors across each fault to calculate offset. Seismic horizons were picked in common-depth-point (CDP) – two-way-time (TWT) (ms) space. CDP spacing is 6.25 m. Seismic horizons were picked so horizons terminate at the fault-reflector intersection, leaving a horizontal gap across each normal-offset fault. The vertical gap is the fault throw in TWT. Where fault drag is apparent, horizons were picked so that the maximum vertical offset of the reflector across a fault is maintained (i.e. extrapolation from either side of a fault unaffected by drag). We are therefore confident that our interpretation represents true vertical separation. The seismic horizons provide a database of TWT picks at every CDP where picks were made.

We convert the fault displacement TWT measurements to metres using seismic interval velocities picked at ~1000 CDP spacing from the original processing of the MCS reflection data by BGR. This is an additional improvement on Geersen et al., (2015), which used a single set of estimated interval velocities throughout the seismic lines.

Around faults of particular interest, we increase the number of interpreted horizons and grid all of the observed vertical separations as a heat map (see Fig. 6 C and G).

3 Results

3.1 Biostratigraphy (from IODP)

Biostratigraphic tie points from the IODP (Fig. 3) borehole data show two distinct periods of sediment deposition in our study area occurring at different rates (McNeill et al., 2017a, 2017b). The age of the oceanic basement is ~68 Ma. Basal materials, dominantly pre-fan pelagic sediments, are ~150 m thick at Site U1480 (Exp. 362 Units III-V) and accumulated at an average rate of ~ 2.5 $mMyr^{-1}$ over the ~60 Myr period from 68 to 9 Ma (rate excluding hiatuses). The overlying Nicobar fan sediments (Exp. 362 Units I-II) are ~1250 m thick at borehole U1480 and accumulated over 9 Myr at an average rate of ~139 $mMyr^{-1}$. Sediment thickness overlaying the oceanic basement increases to ~4km towards the subduction zone due to the influence of plate flexure and filling of the subduction zone trench (SU1, Fig. 2). Most of our isochrones (laterally continuous seismic reflectors) are within the thick fan sediments.

3.2 Fault geometry

Seismic profiles (Figs. 1 and 2) show pervasive fault deformation across an approximately 300 km wide area between the NER and the Sunda subduction zone in the northern part of the Wharton basin. The bathymetric data image the same structures in plan view and indicate a range of orientations, which vary across the oceanic plate. The large number of faults imaged on profiles A and B are roughly evenly distributed from west to east. The fault dip is between 60° and 75° with both landward and seaward dip directions (along-profile). Profile C images sub-vertical faults, which are more heterogeneously distributed from north to south.

We observe numerous lineaments in the multibeam bathymetry data (Fig. 4). We are confident that these lineaments are the surface expression of faults, since they can be tied to faults in the seismic data that displace the seafloor. Lineaments show three distinct orientations between the NER and the Sunda subduction zone that are geographically distinct from each other. We group these lineaments and associated faults into three Classes. Between the NER and ~91° 45’E Class A faults are the dominant fabric, trending NNE-SSW (020-030°); between ~91° 45’E and ~92° 20’E Class B WNW-ESE (100-120°) lineaments dominate; and ~between 92° 20’E and 93° Class C N-S (350-010°) dominate. It is unclear whether the Class A and B fabrics overprint each other, but in the area of Class B faulting, very few NNE-SSW faults are observed in the bathymetry suggesting that there is a genuine change from one orientation to the other. In the area of Class C faulting, Class A and B fault orientations are effectively absent. The N-S trending faults (Class C) are in good agreement with both the position and orientation of previously mapped Wharton Ridge fossil fracture zones (e.g. Singh et al., 2011).

3.3 Class A faults

Class A faults are only observed on seismic profile C in the west of our study area (Fig. 1). They are sub-vertical, propagate through the entire sedimentary section and deform the oceanic basement. The sense of displacement is unclear, sedimentary layers frequently show a v-shaped pattern that is expressed at the seafloor (Fig. 5A, B). We also note differences in sedimentary layer thickness across these faults and complex displacement patterns that indicate both apparent normal and reverse displacement (Fig. 5C). These features are very similar to interpreted strike-slip faults at the NER (Sager et al., 2013) and strike-slip faults in general. The complex displacement profiles for these faults limits our ability to constrain the timing of their formation and subsequent activity.

3.4 Class B faults

Class B faults are imaged by seismic profiles A and B, making up the majority of faults on these profiles. Class B faults form structures of conjugate normal faults that converge at depth within the sedimentary section, showing little to no offset at or below reflector R12 (e.g. Fig. 6, E and F). Typically, a central pair of faults that reach the seabed meet at around 1.5 s TWT below seafloor (~1800-2000 mbsf) in the vicinity of reflector R10 (8.6 Ma). One or both of these central faults may penetrate the entire sediment section, but die out before or very shortly after reaching the top of the oceanic basement. The central pair of faults are surrounded by multiple, typically 10-20, seismically-resolvable faults, with a roughly even distribution between seaward- and landward-dipping geometries. These minor faults include multiple blind faults that branch from the central pair (hard-linked) and faults that are just spatially related (soft-linked). The number of blind faults increases below reflector R5 (2.6 Ma), but then decreases below reflector R10. Gridded displacement for Class B conjugate fault groups (example in Fig. 6 G) shows that the more vertically extensive faults dominate, but that maximum displacement is concentrated in the middle of the sediment section, decreasing up- and down-section. This depth-displacement relationship is maintained when all the faults in the group are summed together (Fig. 6 H). We suggest that this is the result of purely strike-slip motion on a sub-vertical plane at depth expressed as extension in the surface cover, therefore requiring vertical displacement to decrease downwards, and that the upward decrease indicates continuous activity started at where maximum displacement is observed (Fig. 6 I).

3.5 Class C faults

Class C faults are only observed in the eastern part of our study area (on seismic profiles A and B) and are spatially related to significant basement topography. Anomalous basement highs - long-wavelength (~20 km wide), topographic changes of 0.6-0.8 s of TWT (approx. 900-1200 m) - are also coincident with the locations of Wharton Ridge fracture zones (e.g. Jacob et al., 2014). In the seismic data these basement anomalies show a different character to seamounts; seamounts are shorter wavelength (~5 km wide), more acoustically transparent, and show up-warping of the adjacent and overlaying sedimentary layers (e.g. at ~160 km along profile, Fig. 2). We also note that across the basement anomalies, we observed the same, strongly reflective, seismic character as at the top of the oceanic basement, whereas the top of seamounts are less reflective.

We attribute all Class C faults observed in the seismic data within the extents of basement anomalies to be structurally related to the major fracture zones. Within these zones there are 3-6 seafloor to basement faults, with up to 50 minor blind faults. The number of blind faults increases with depth in the section, with a marked increase at reflector R5 (2.6 Ma). Unlike Class B faults, the number of blind faults does not decrease below reflector R10 (8.6 Ma). Displacement across Class C faults (e.g. Fig 6 C, top panel) shows that individually, blind faults have minor vertical offset, and that seafloor-to-basement faults dominate. When all faults within each Class C structure are summed, the displacement increases with depth to at least reflector R11 (9.3 Ma) (e.g. Fig 6 D, bottom panel). However, this trend does not necessarily continue down to basement, and displacement appears to be less at reflector R12 (14.4 Ma) for the basement anomalies that relate to fracture zone F7 (Fig 7 B).

The bathymetric trace above and extrapolated north-south from the seismic Class C faults (see S3 supplementary material) shows an overall N-S trend, but is composed of en-echelon NW-SE normal faults. In places, NW-SE faults form small pull-apart basins, indicating left-lateral motion.

3.6 Class D faults

On NW-SE profile C (Fig. 1), we find evidence of reverse faulting and associated fault-propagation folding. These Class D faults are buried by the youngest sediments with no surface trace in the bathymetry data, therefore we cannot confirm their orientation. Since we do not image these features on the WSW-ENE seismic profiles A and B (Fig. 1), we infer they strike broadly. ~NE-SW to E-W, in agreement with Abercrombie et al., 2003. Maximum compression in the Wharton basin is ~NW-SE (Gordon and Houseman, 2015), and Hananto et al. (2018) observed ENE-WSW bathymetric features associated with thrust faults to the south of our study area. This is a clear contrast with the dominant E-W trending reverse faults west of the NER (between 78° E and 82° E) (Bull, 1990; Bull and Scrutton, 1992, 1990; Krishna et al., 2001). In addition, we observe buried, high-angle (65-70°) normal faults in profile C that offset the oceanic basement (not observed on profiles A and B).

The warping of sedimentary horizons due to reverse folding (Fig. 8) affects most/all of the sedimentary section, starting at the top of the oceanic basement, and decreasing in amplitude upward, suggesting recent activity. We observe growth strata in the hanging wall onlapping onto the crest of the fault-propagation folds. The occurrence of onlap is not continuous, but is concentrated onto reflector R8 (7.2 Ma) and onto a horizon in the interval reflectors R7 (5.8 Ma) and R6 (3.5 Ma) (arrows, Fig. 8). Onlap/growth strata are visible deeper than reflector R8, i.e. older than 7.2 Ma, however, our ability to constrain earlier activity is limited by the quality and resolution of the seismic data, and basement topography between the IODP drill sites and the locations of Class D faults obscuring sedimentary horizons. Above reflector R8 where we observe no onlap, thickness is generally maintained suggesting activity was discontinuous.

3.7 Fault displacement and dip direction variations from the NER to the Subduction Zone

Overall trends in fault displacement were analysed along seismic profiles A and B to determine its variation with proximity to the subduction zone. We split displacement measurements into landward- and seaward-dipping fault polarities for each reflector, with positive values for landward-dipping fault displacements and negative for seaward-dipping. The polarity of cumulative displacement therefore reflects the dominance of landward- (positive) versus seaward-dipping (negative) faults. For each reflector analysed (R2-12), this differential cumulative displacement (e.g., Fig. 9A) shows an overall positive increase towards the subduction zone hence a net dominance of landward-dipping faults. However, there is variation between reflectors. Reflectors R7-9 (~6 – 8 Ma) show the greatest increase in displacement towards the subduction zone, on both landward- and seaward-dipping geometries, and are the same reflectors where maximum displacement is most commonly observed on Class B faults.

Since faults are roughly evenly distributed west to east, we can group faults and sum displacement for each reflector (R2-12) for overlapping 20 km segments along profile to show how displacement with depth varies across the Wharton Basin (Fig. 9 B). This shows peak displacement close to the NER is in the middle of the section, , increasing roughly linearly with depth towards the east, approaching the subduction zone. However, fracture zone structures in the eastern part of the section, with specific displacement patterns, may bias this result. We observe no significant difference in the depth-displacement profiles of landward- versus seaward-dipping faults.

3.8 Relationships between seismic and core-scale faulting and sediment material properties

For each 20 km segment on seismic profiles A and B, we normalise the depth-displacement profile against the corresponding maximum displacement (black line, Fig. 7A). This allows us to directly compare the pattern of displacement with depth for each 20 km segment with the IODP borehole data. By adjusting the depths of the seismic reflectors (R2-12) to Site U1480, we can plot fault displacement against various datasets from the borehole (i.e. lithology, sand fraction, age-depth relationship, fracture intensity, seismic velocity and porosity, see S4 supplementary material). Figure 7A shows the overall average displacement of the 20 km segments (black line) and examples (coloured lines) from detailed analyses (e.g. as shown in Fig. 6 E-H). There is a linear increase in displacement with depth down to reflector R7 (5.8 Ma), however the patterns are bell-shaped, showing maximum displacement in the middle of the sediment section, mostly between reflectors R7 and R10 (5.8 and 8.6 Ma, 600-1100 mbsf in borehole U1480). The overall average shows maximum displacement at reflector R8 (7.2 Ma), at borehole depth ~800 mbsf close to the lithological IIB-IIC subunit boundary, which represents a general downhole reduction in sand content (McNeill et al., 2017b).

There is some correlation between the increased frequency of faults in cores with the mid-section zone of increased seismic-scale fault displacement (Fig. 7A and B). No faults were observed in cores shallower than 400 mbsf (reflector R6), but a significant number were observed between reflectors R6 (3.5 Ma) and R10 (8.6 Ma) (400-1100 mbsf). Between reflector R10 (8.6 Ma) and R12 (14.4 Ma) (~ 1100 and ~1300 mbsf), no core faults were observed. We observe no other correlation between seismic-scale fault structure/displacement and other material properties, e.g., velocity, porosity.

4 Discussion

We find four distinct, mostly still active, fault sets in the northern Wharton Basin formed in response to the regional stress field and influenced by combinations of proximity to the Sunda subduction zone and compressional deformation related to continental collision.

4.1 Fault sets across the northern Wharton Basin

- Class A: NNE-SSW (020-030°) trending, sub-vertical strike-slip faults observed between the Ninety East Ridge (NER) and 91°45’ E.
- Class B: WNW-ESE (100-120°) trending, high-angle (65-70°) conjugate normal faults forming flower structures in the sedimentary section in response to strike-slip motion, observed between 91°45’ E and 92°20’E.
- Class C: N-S (350-010°) trending, high angle (65-75°) faults with normal displacement, associated with long-wavelength (~20 km wide) basement topography.

Interpreted as related to left-lateral motion along pre-existing fracture zones. Observed between 92°20'E and the Sunda subduction zone.

- Class D: Reverse faults and associated fault-propagation folding that may reactivate pre-existing crustal spreading fabric. Precise fault orientation cannot be resolved but a likely range of E-W to NE-SW.

4.2 Activity history of intraplate strike-slip faulting in the Wharton Basin

Previous interpretations of fault activity in the Wharton Basin suggested that intraplate deformation began around 40 Ma, and increased in intensity around 20 Ma (e.g. Geersen et al., 2015). However, new chronostratigraphic information now allows us to determine timings. Geersen et al. (2015) and Singh et al. (2017) both noted increasing displacement with depth on N-S trending faults that correlate with fracture zone positions, and interpreted continuous activity since at least the time of deposition of the deepest sediments.

N-S faults (Class C), have similar surface traces and positions to fracture zones F6 and F7 (nomenclature from Singh et al., 2011). Seafloor deformation from Class C faults includes pull-apart basins and NW-SE en-echelon lineations, indicating left-lateral slip and confirming current activity, observed from 3°15'N to at least 4°N. We therefore suggest that our Class C faults are the northward continuation of fracture zones F6 and F7. Displacements on Class C faults increases with depth to reflector R11 (9.3 Ma), and apparent offsets at the top of oceanic basement are ~400 m, somewhat consistent with the analysis by Carton et al. (2014) and Singh et al. (2017) for the same structures. The age of oceanic basement in our study area is ~68 Ma (Jacob et al., 2014), increasing displacement with depth suggests continuous activity through the deposition of the sedimentary sequence. However, the highly condensed sedimentary section below reflector R11 prevents confirming an increase in displacement down to basement, and reduces our ability to constrain the timing of activity through this period (basement formation and the onset of Nicobar Fan deposition) as precisely. Near fracture zone F7, there is a down-section decrease in displacement between reflectors R11 (9.3 Ma) and R12 (14.4 Ma) (Fig. 7B). Therefore we suggest activity (on at least this structure, and possibly also fracture zone F6) began between 9.3 and 14.4 Ma, broadly consistent with the onset of intraplate activity at 14-15.5 Ma suggested by Bull et al. (2010) and Krishna et al. (2009) from faulting west of the NER.

Displacement profiles for Class A and B faults differ significantly from Class C fracture-zone-faults. Class A faults do show evidence of basement deformation or offset, but no consistent trend in displacement/vertical separation down-section (e.g. Fig. 5). This may be due to their significant strike-slip component with changing vertical displacement over time, there may also be an element of apparent thickness change due to juxtaposition through strike-slip motion (e.g. Sager et al., 2013). We therefore can confirm current activity but cannot confidently constrain their initiation or activity history. In contrast, Class B faults do show a consistent trend in their displacement profiles; they generally do not offset the oceanic basement, and displacement is maximum in the middle of the sedimentary section, decreasing both upward and downward (Figs. 6E-H and 7A). Geersen et al. (2015) previously suggested that this pattern was caused by fault nucleation in the middle of the sedimentary section and subsequent propagation up and down. Decreasing displacement upwards suggests syn-tectonic deposition and continued activity. Decreasing displacement downwards below the position of maximum displacement is more difficult to explain, however, we suggest that Class B faults represent the shallow expression of a deeper, purely strike-slip shear zone: a sub-vertical WNW shear zone in the upper mantle and crust, as exemplified by the 2012 earthquakes, induces extension in the sedimentary cover which is accommodated by en-échelon normal faults that form negative flower structures or wrench faults (Wilcox et al., 1973). The shallow faults in the sedimentary cover (which we resolve as Class B faults) may or may not be hard-linked to the deeper shear plane, but since there is a discrepancy in the sense of displacement – normal to strike slip – by necessity vertical offset must gradually die out at depth as a greater proportion of displacement is accommodated by strike-slip motion (see Fig. 6 I). Sediment compaction cannot account for the decreasing displacement pattern with depth, because significant growth strata are not observed and displacement decrease on these faults is significantly more than the 20% of maximum suggested reasonable for compaction (Taylor et al., 2008). Therefore we agree with Geersen et al. (2015) that the position of maximum displacement (reflector R8 ~7.2 Ma) indicates the initiation timing of Class B deformation. This is consistent with the timing of acceleration of rotation/convergence between the Indian and Capricorn sub-plates (Fig. 7 A and D) (Bull et al., 2010; DeMets et al., 2010) and the intensification of compressional deformation west of the NER (Fig. 7 C) (Krishna et al., 2009, 2001). We use Capricorn-India rotation as a proxy here due to the present lack of accurate plate reconstructions for India-Australia rotation, which would be more directly relevant. We suggest that compressional deformation west (and east, (see below)) of the NER and Class B faulting east of the NER were intensified/initiated by the same tectonic event. Uplift of the Tibetan Plateau is often invoked as such an event (e.g. Bull et al., 2010), but we also acknowledge that recent work has linked Indian Ocean deformation to changes in mantle upwelling at the Reunion hotspot, independent of the Tibetan Orogeny (Iaffaldano et al., 2018).

4.3 Compressional deformation in the Wharton Basin

Our Class D faults confirm compressional deformation in the Wharton basin, as suggested by Hananto et al. (2018), in addition to the more widely recognised strike-slip deformation. Although Class D faults are mostly blind, folding is evident at reflector R4 (Fig. 8), suggesting activity at least as recent as 2.2 Ma. We suggest a likely NE-SW to E-W orientation for these faults, consistent with observations to the south of our area (Hananto et al., 2018) and west of the NER (e.g. Bull, 1990; Bull and Scrutton, 1992, 1990; Krishna et al., 2001). Bull (1990) suggested that the spacing, E-W orientation (orthogonal to oceanic transforms) and basement offsets of the reverse faults west of the NER indicates that they are reactivated spreading-ridge normal faults. Buried, inactive normal faults we observe in the Wharton Basin (labelled on Fig. 8), may be Wharton Ridge spreading fabric, with Class D faults similarly reactivating this.

West of the NER, fold-related growth strata onlaps onto a 7-8 Ma unconformity (Bull and Scrutton, 1992; Krishna et al., 2001) and onto younger unconformities at 4-5 Ma, and 0.8 Ma (Krishna et al., 2001), interpreted as three phases of deformation, with 3-4 m.y. cyclicity and) limited activity prior to 8 Ma. For Class D faults east of the NER, we observe growth strata below reflector R8 (7.2 Ma; Fig. 8), but lack deeper age-controlled reflectors, so can only confirm that reverse faulting east of the NER initiated by 7.2 Ma. Specifically, onlap onto reflector R8 (7.2 Ma),onto a horizon between reflectors R7 (5.8 Ma) and R6 (3.5 Ma), and onto reflector R4 (2.2 Ma) (Fig. 8). Across-fault layer thickness is otherwise maintained between reflectors suggesting discrete phases of fault activity at 7-8 Ma,4-5 Ma and possibly ~2 Ma. This may indicate broadly contemporaneous timing of compressional deformation west and east of the NER, although we do not find evidence for deformation occurring ca. 0.8 Ma in the Wharton Basin, east of the NER. We also acknowledge that the onlap patterns between R7 and R6 may equally be the result of changes in sediment accumulation rates (Fig. 3), since there is no indication of plate motion changes around 4-5 Ma (Fig. 7D) (Bull et al., 2010).

4.4 Strike-slip related fault patterns and mechanisms

The three fault Classes with seafloor expression (Classes A to C) appear to define a strike-slip Riedel shear pattern. Riedel shearing on 10-100s km scale in the Wharton basin has previously been suggested by both Geersen et al. (2015) and Hananto et al. (2018), where the principal displacement is left-lateral slip on the N-S reactivated fracture zones. However, Geersen et al. (2015) did not identify our Class B faults (we attribute this to our reprocessing of the multibeam data clarifying surface orientations) and Hananto et al. (2018) apparently misinterpret NNE-SSW left-lateral faults (our Class A fault equivalents) as R shears, when this orientation and displacement would represent P shears if forming in response to left-lateral N-S principal slip (e.g. Davis et al., 2000; Dresen, 1991). There is clear evidence that the system we observe in the Wharton Basin is left-lateral (e.g. Deplus et al., 1998; Duputel et al., 2012; Geersen et al., 2015).

To resolve and integrate our new and existing fault observations, we compiled all interpreted seafloor lineations in the region into a fault map (Fig. 10A) demonstrating that the same fabrics we observe are present across the entire northern Wharton basin, and to some extent onto the NER (this study; Hananto et al., 2018; Sager et al., 2013). The fault/lineation orientations are: 020-030° (left-lateral, Class A); 100-120° (right-lateral, Class B) and 350-010° (left-lateral, Class C). Singh et al. (2017) showed that lineations orientated 100-120°, i.e. equivalents of our Class B faults, are right-lateral shear zones composed of NW-SE trending, en-echelon normal faults (also see Fig. 6 I). If Class C faults represent the principal displacement zone (PDZ), Class A faults are ~+25° (R) and Class B faults are ~-70° (R’), together consistent with Riedel shearing.

The 2012 >M_w 8 earthquakes, were complex, rupturing a primary WNW-trending fault (286-289°), parallel to our Class B faults, and a secondary NNE-trending fault (016-020°), in good agreement with our Class A fault orientations (Wei et al., 2013; Yue et al., 2012). But the earthquakes do not appear to have ruptured the Class C (N-S reactivated fracture zone) fault type. Hill et al. (2015) suggested the discrepancy between the NNE-trending rupture plane and the N-S fracture zones could indicate rupture on a set of en-echelon, right-stepping sub-segments of the fracture zone.

If we instead consider the NNE-trending fault rupture as the PDZ at depth and not the N-S fracture zone, the fault orientations at the surface all fit a Riedel shear pattern (Fig. 10C). The new PDZ is left-lateral and orientated NNE-SSW, 016-020°: NNE-trending Class A faults are left-lateral P or Y shears (+0-14°); WNW-trending Class B faults are right-lateral R' shears (-76-90°), and N-S trending Class C faults (i.e. fracture zone faults) are left-lateral R shears (-5-25°). Therefore, the reactivated fracture zones in the Wharton basin make up right-stepping R shears, and pervasive Class B faults represent the linkage between them. The primary WNW-trending 2012 rupture plane may have been in response to a stress difference across the transfer zones between the major fracture zones, rupturing along Class B faults/shears and with associated NNE fault rupture along Class A faults (P- or Y-shears).

This fault structural (Riedel) pattern is also consistent with our observed sequence of fault activity. We propose that initial intraplate deformation began between ~14 and ~15.5 Ma as suggested by Bull et al., (2010) and the displacement pattern shown by Class C faults. Intraplate convergence may have reactivated Wharton Ridge fracture zones forming Class C faults (R shears) in response to NNE-SSW shearing, with an acceleration of Indian-Australian convergence (contemporaneous with Indian-Capricorn acceleration (Dean et al., 2010), Fig. 7 D) intensifying deformation in the Wharton Basin and initiating Class B faults (R' shears) in the transfer zones between fracture zones at this time. At ~7 Ma, activity on fracture zones F6 and F7 appears to have decreased or stopped (Fig. 7 B) and that strain was transferred to the developing set of Class B faults at this time. This could be due to strain weakening of the plate at depth, whereby ~7 Ma represents a time when the plate has weakened so that deformation becomes a lot less localised on the pre-existing fabric (fracture zones), allowing Class B faults to form (Delescluse et al., 2008).

4.5 Changes in deformation from the Ninety East Ridge to the Sunda subduction zone

The discrete fault sets occur in distinct geographic areas across the northern Wharton Basin (Fig. 10A). We suggest this is compatible with Class B faults forming R' shears and therefore only developing in the zones between the fracture zones (Class C faults). This geographic change in faulting explains the change in displacement with depth from west to east (Fig. 9 C): the west is dominated by Class B faults with maximum displacement in the middle of the sedimentary section, the east by Class C faults, with displacement increasing with depth (Fig. 6 A-H, Fig7A, B).

Common across all of the strike-slip related faults (Class A-C) we observe is the dominance of E-dipping faults (landward or towards the subduction zone) due to greater average displacement rather than number of each fault type (Fig. 9A). We suggest that since these faults have near exclusively normal displacement in cross-section, increased landward-dipping fault displacement could be amplified by plate bending toward the subduction zone. Although these faults appear to be composed of NW-SE-trending en-echelon faults, we cannot confirm they are parallel to the subduction zone. Similarly, Graindorge et al. (2008) argued that plate bending within our study area is accommodated by a range of fault orientations including N-S.

4.6 Relationship between fault displacement patterns at a range of scales and material properties

The lithology and porosity of the oceanic plate sediments (IODP Expedition 362; McNeill et al., 2017b) do not appear to correlate with the fault activity or depth-displacement patterns. This suggests the most important factor controlling fault initiation and development is an external driving force. Here we propose that driver is the onset and acceleration of plate convergence between Indian and Australia (Bull et al., 2010; G. Iaffaldano et al., 2018).

For Class B faults, the position of maximum seismic-scale fault displacement (middle of the sedimentary section, reflector R8, 7.2 Ma) matches a concentration of core-scale fractures (between reflectors R6, 3.5 Ma, and R10, 8.6 Ma) (Fig. 7A). In addition, an apparent upward increase in sand content (subunit IIB-IIC boundary; McNeill et al., 2017b) occurs at this depth (see S4 supplementary material). We postulate that increased core-fracture intensity reflects Class B fault nucleation and development, while variations in sediment material properties do not affect the tectonic history.

5 Conclusions

- Four distinct styles of faulting (Classes A to D) occur in the northern Wharton Basin (equatorial Indian Ocean), with all structures potentially active.
- Shortening within the diffuse plate boundary zone due to convergence between the Australian and Indian plates caused the development of N-S trending Class C faults, with their initiation contemporaneous with the onset of compressional deformation west of the Ninety-east Ridge (ca. 14 Ma). Original spreading-centre formed normal faults were reactivated by the later compression to form the E- to NE-trending Class D reverse faults.
- An acceleration in the convergence between Indian and Australia ~7-9 Ma intensified deformation in the Wharton Basin, initiating a new set of faults (WNW-trending Class B faults, and probably NNE-trending Class A faults) that define a Riedel shear pattern, where the principal displacement direction is NNE-SSW left-lateral. N-S trending reactivated fracture zones (and Class C faults) act as synthetic R-shears, WNW-trending Class B faults are antithetic R'-shears, and N-S trending Class A

faults are either synthetic P-shears or Y-shears. This structural style is reflected by the 2012 earthquakes, with the main fault rupture along WNW-trending Class B faults, possibly resulting from stress transfer between individual reactivated fracture zones.

- Class B and C faulting may be partly driven by subduction-related Indo-Australian plate bending. This process has favoured displacement on landward-dipping faults.
- Lithological variations within the Nicobar Fan sediments do not control the development of distributed seismic-scale faulting, however, there is a correlation between fracture intensity observed in sediment cores, and periods of increased deformation.

6 Acknowledgements

This research used data provided by the International Ocean Discovery Program (IODP) (www.iodp.org/access-data- and-samples) and was supported by the Natural Environmental Research Council [grant numbers NE/P012817/1 and NE/L002531/1]. We thank the JOIDES Resolution crew, IODP technical team and science party for their contributions during Expedition 362. We also thank Dave Sanderson for useful discussions, the two anonymous reviewers for their comments, which helped to improve this manuscript and editor Jean-Philippe Avouac.

7 References

Abercrombie, R.E., Antolik, M., Ekström, G., 2003. The June 2000 Mw 7.9 earthquakes south of Sumatra: deformation in the India–Australia plate. J. Geophys. Res. Solid Earth 108, ESE-6.

Bergman, E.A., Solomon, S.C., 1985. Earthquake source mechanisms from body-waveform inversion and intraplate tectonics in the northern Indian Ocean. Phys. Earth Planet. Inter. https://doi.org/10.1016/0031-9201(85)90002-0

Bull, J.M., 1990. Structural style of intra-plate deformation, Central Indian Ocean Basin: evidence for the role of fracture zones. Tectonophysics. https://doi.org/10.1016/0040-1951(90)90054-C

Bull, J.M., DeMets, C., Krishna, K.S., Sanderson, D.J., Merkouriev, S., 2010. Reconciling plate kinematic and seismic estimates of lithospheric convergence in the central Indian Ocean. Geology 38, 307–310. https://doi.org/10.1130/G30521.1

Bull, J.M., Scrutton, R.A., 1992. Seismic reflection images of intraplate deformation, central Indian Ocean, and their tectonic significance. J. Geol. Soc. London. 149, 955–966. https://doi.org/10.1144/gsjgs.149.6.0955

Bull, J.M., Scrutton, R.A., 1990. Fault reactivation in the central Indian Ocean and the rheology of oceanic lithosphere. Nature. https://doi.org/10.1038/344855a0

Carton, H., Singh, S.C., Hananto, N.D., Martin, J., Djajadihardja, Y.S., Franke, D., Gaedicke, C., 2014. Deep seismic reflection images of the Wharton Basin oceanic crust and uppermost mantle offshore Northern Sumatra: Relation with active and past deformation. J. Geophys. Res. Solid Earth 119, 32–51.

Chamot-Rooke, N., 1993. Intraplate shortening in the central Indian Ocean determined from a 2100-km-long north-south deep seismic reflection profile. Geology 21, 1043–1046. https://doi.org/10.1130/0091-7613(1993)021<1043:ISITCI>2.3.CO;2

Clift, P.D., Hodges, K. V, Heslop, D., Hannigan, R., Van Long, H., Calves, G., 2008. Correlation of Himalayan exhumation rates and Asian monsoon intensity. Nat. Geosci. 1, 875.

Copley, A., Avouac, J., Royer, J., 2010. India-Asia collision and the Cenozoic slowdown of the Indian plate: Implications for the forces driving plate motions. J. Geophys. Res.

Solid Earth 115.

Davis, G.H., Bump, A.P., García, P.E., Ahlgren, S.G., 2000. Conjugate Riedel deformation band shear zones. J. Struct. Geol. 22, 169–190. https://doi.org/10.1016/S0191-8141(99)00140-6

Dean, S.M., McNeill, L.C., Henstock, T.J., Bull, J.M., Gulick, S.P.S., Austin, J.A., Bangs, N.L.B., Djajadihardja, Y.S., Permana, H., 2010. Contrasting décollement and prism properties over the Sumatra 2004–2005 earthquake rupture boundary. Science (80-.). 329, 207–210.

Delescluse, M., Montési, L.G.J., Chamot-Rooke, N., 2008. Fault reactivation and selective abandonment in the oceanic lithosphere. Geophys. Res. Lett. 35.

DeMets, C., Gordon, R.G., Argus, D.F., 2010. Geologically current plate motions. Geophys. J. Int. 181, 1–80.

DeMets, C., Gordon, R.G., Argus, D.F., Stein, S., 1990. Current plate motions. Geophys. J. Int. 101, 425–478.

DeMets, C., Gordon, R.G., Royer, J.-Y., 2005. Motion between the Indian, Capricorn and Somalian plates since 20 Ma: implications for the timing and magnitude of distributed lithospheric deformation in the equatorial Indian ocean. Geophys. J. Int. 161, 445–468.

Deplus, C., 2001. Indian ocean actively deforms. Science (80-.). 292, 1850–1851. https://doi.org/10.1126/science.1061082

Deplus, C., Diament, M., Hébert, H., Bertrand, G., Dominguez, S., Dubois, J., Malod, J., Patriat, P., Pontoise, B., Sibilla, J.J., 1998. Direct evidence of active deformation in the eastern Indian oceanic plate. Geology 26, 131–134. https://doi.org/10.1130/0091-7613(1998)026<0131:DEOADI>2.3.CO;2

Dresen, G., 1991. Stress distribution and the orientation of Riedel shears. Tectonophysics 188, 239–247. https://doi.org/10.1016/0040-1951(91)90458-5

Duputel, Z., Kanamori, H., Tsai, V.C., Rivera, L., Meng, L., Ampuero, J.P., Stock, J.M., 2012. The 2012 Sumatra great earthquake sequence. Earth Planet. Sci. Lett. 351–352, 247–257. https://doi.org/10.1016/j.epsl.2012.07.017

Geersen, J., Bull, J.M., McNeill, L.C., Henstock, T.J., Gaedicke, C., Chamot-Rooke, N., Delescluse, M., 2015. Pervasive deformation of an oceanic plate and relationship to large > Mw8 intraplate earthquakes: The northern Wharton Basin, Indian Ocean. Geology 43, 359–362. https://doi.org/10.1130/G36446.1

Gordon, R.G., 2009. Lithospheric deformation in the equatorial Indian Ocean: Timing and Tibet. Geology 37, 287–288.

Gordon, R.G., DeMets, C., Royer, J.Y., 1998. Evidence for long-term diffuse deformation of the lithosphere of the equatorial Indian Ocean. Nature 395, 370–374. https://doi.org/10.1038/26463

Gordon, R.G., Houseman, G.A., 2015. Deformation of Indian ocean lithosphere: Evidence for a highly nonlinear rheological law. J. Geophys. Res. Solid Earth 120, 4434–4449. https://doi.org/10.1002/2015JB011993

Graindorge, D., Klingelhoefer, F., Sibuet, J.C., McNeill, L., Henstock, T.J., Dean, S., Gutscher, M.A., Dessa, J.X., Permana, H., Singh, S.C., Leau, H., White, N., Carton, H., Malod, J.A., Rangin, C., Aryawan, K.G., Chaubey, A.K., Chauhan, A., Galih, D.R., Greenroyd, C.J., Laesanpura, A., Prihantono, J., Royle, G., Shankar, U., 2008. Impact of lower plate structure on upper plate deformation at the NW Sumatran convergent margin from seafloor morphology. Earth Planet. Sci. Lett. 275, 201–210. https://doi.org/10.1016/j.epsl.2008.04.053

Hananto, N., Boudarine, A., Carton, H., Singh, S.C., Avianto, P., Dyment, J., Qin, Y., Ghosal, D., Zuraida, R., Tapponnier, P.E., 2018. Evidence of pervasive trans-tensional deformation in the northwestern Wharton Basin in the 2012 earthquakes rupture area. Earth Planet. Sci. Lett. 502, 174–186.

Hill, E.M., Yue, H., Barbot, S., Lay, T., Tapponnier, P., Hermawan, I., Hubbard, J., Banerjee, P., Feng, L., Natawidjaja, D., Sieh, K., 2015. The 2012 Mw 8.6 Wharton Basin sequence: A cascade of great earthquakes generated by near-orthogonal, young, oceanic mantle faults. J. Geophys. Res. Solid Earth 120, 3723–3747. https://doi.org/10.1002/2014JB011703

Iaffaldano, G., Davies, D.R., Demets, C., 2018. Indian Ocean floor deformation induced by the Reunion plume rather than the Tibetan Plateau. Nat. Geosci. 11, 362–366. https://doi.org/10.1038/s41561-018-0110-z

Jacob, J., Dyment, J., Yatheesh, V., 2014. Revisiting the structure, age, and evolution of the Wharton Basin to better understand subduction under Indonesia. J. Geophys. Res. Solid Earth 119, 169–190. https://doi.org/10.1002/2013JB010285

Krishna, K.S., Bull, J.M., Scrutton, R.A., 2009. Early (pre-8 Ma) fault activity and temporal strain accumulation in the central India Ocean. Geology 37, 227–230. https://doi.org/10.1130/G25265A.1

Krishna, K.S., Bull, J.M., Scrutton, R.A., 2001. Evidence for multiphase folding of the central Indian Ocean lithosphere. Geology 29, 715–718.

Liu, C.-S., Curray, J.R., McDonald, J.M., 1983. New constraints on the tectonic evolution of the eastern Indian Ocean. Earth Planet. Sci. Lett. 65, 331–342. https://doi.org/10.1016/0012-821X(83)90171-1

McNeill, L.C., Dugan, B., Backman, J., Pickering, K.T., Pouderoux, H.F.A., Henstock, T.J., Petronotis, K.E., Carter, A., Chemale, F., Milliken, K.L., Kutterolf, S., Mukoyoshi, H., Chen, W., Kachovich, S., Mitchison, F.L., Bourlange, S., Colson, T.A., Frederik, M.C.G., Guèrin, G., Hamahashi, M., House, B.M., Hüpers, A., Jeppson, T.N., Kenigsberg, A.R., Kuranaga, M., Nair, N., Owari, S., Shan, Y., Song, I., Torres, M.E., Vannucchi, P., Vrolijk, P.J., Yang, T., Zhao, X., Thomas, E., 2017a. Understanding Himalayan erosion and the significance of the Nicobar Fan. Earth Planet. Sci. Lett. 475, 134–142. https://doi.org/10.1016/j.epsl.2017.07.019

McNeill, L.C., Dugan, B., Petronotis, K.E., Backman, J., Bourlange, S., Chemale, F., Chen, W., Colson, T.A., Frederik, M.C.G., Guèrin, G., Hamahashi, M., Henstock, T., House, B.M., Hüpers, A., Jeppson, T.N., Kachovich, S., Kenigsberg, A.R., Kuranaga, M., Kutterolf, S., Milliken, K.L., Mitchison, F.L., Mukoyoshi, H., Nair, N., Owari, S., Pickering, K.T., Pouderoux, H.F.A., Yehua, S., Song, I., Torres, M.E., Vannucchi, P., Vrolijk, P.J., Yang, T., Zhao, X., 2017b. Expedition 362 summary. Proc. Int. Ocean Discov. Progr. 362, 21–22. https://doi.org/10.7289/V5C8276M

Merkouriev, S., DeMets, C., 2006. Constraints on Indian plate motion since 20 Ma from dense Russian magnetic data: Implications for Indian plate dynamics. Geochemistry, Geophys. Geosystems 7. doi:10.1029/2005GC001079

Molnar, P., England, P., Martinod, J., 1993. Mantle dynamics, uplift of the Tibetan Plateau, and the Indian monsoon. Rev. Geophys. 31, 357–396.

Molnar, P., Stock, J.M., 2009. Slowing of India’s convergence with Eurasia since 20 Ma and its implications for Tibetan mantle dynamics. Tectonics 28.

Sager, W.W., Bull, J.M., Krishna, K.S., 2013. Active faulting on the Ninetyeast ridge and its relation to deformation of the Indo-Australian plate. J. Geophys. Res. Solid Earth 118, 4648–4668.

Singh, S.C., Carton, H., Chauhan, A.S., Androvandi, S., Davaille, A., Dyment, J., Cannat, M., Hananto, N.D., 2011. Extremely thin crust in the Indian Ocean possibly resulting from Plume-Ridge Interaction. Geophys. J. Int. 184, 29–42. https://doi.org/10.1111/j.1365-246X.2010.04823.x

Singh, S.C., Hananto, N., Qin, Y., Leclerc, F., Avianto, P., Tapponnier, P.E., Carton, H., Wei, S., Nugroho, A.B., Gemilang, W.A., Sieh, K., Barbot, S., 2017. The discovery of a conjugate system of faults in the wharton basin intraplate deformation zone. Sci. Adv. 3, 1–9. https://doi.org/10.1126/sciadv.1601689

Stein, C.A., Cloetingh, S., Wortel, R., 1989. Seasat-derived gravity constraints on stress and deformation in the northeastern Indian Ocean. Geophys. Res. Lett. https://doi.org/10.1029/GL016i008p00823

Stein, C.A., Weissel, J.K., 1990. Constraints on the Central Indian Basin thermal structure from heat flow, seismicity and bathymetry. Tectonophysics. https://doi.org/10.1016/0040-1951(90)90076-K

Stein, S., Okal, E.A., 1978. Seismicity and tectonics of the Ninetyeast Ridge Area: Evidence for internal deformation of the Indian Plate. J. Geophys. Res. https://doi.org/10.1029/JB083iB05p02233

Sykes, L.R., 1970. Seismicity of the Indian Ocean and a possible nascent island arc between Ceylon and Australia. J. Geophys. Res. https://doi.org/10.1038/nprot.2012.101

Taylor, S.K., Nicol, A., Walsh, J.J., 2008. Displacement loss on growth faults due to sediment compaction. J. Struct. Geol. 30, 394–405.

Wei, S., Helmberger, D., Avouac, J., 2013. Modeling the 2012 Wharton basin earthquakes off-Sumatra: Complete lithospheric failure. J. Geophys. Res. Solid Earth 118, 3592–3609.

Weissel, J.K., Anderson, R.N., Geller, C.A., 1980. Deformation of the Indo-Australian plate. Nature 287, 284–291. https://doi.org/10.1038/287284a0

Wiens, D.A., Stein, S., Demets, C., Gordon, R.G., Stein, C., 1986. Plate tectonic models for Indian Ocean “intraplate” deformation. Tectonophysics. https://doi.org/10.1016/0040-1951(86)90023-5

Wilcox, R.E., Harding, T.P., Seely, D.R., 1973. Basic wrench tectonics. Bull. AAPG 57, 74–96.

Yue, H., Lay, T., Koper, K.D., 2012. En échelon and orthogonal fault ruptures of the 11 April 2012 great intraplate earthquakes. Nature 490, 245–249. https://doi.org/10.1038/nature11492

8 Figures and captions

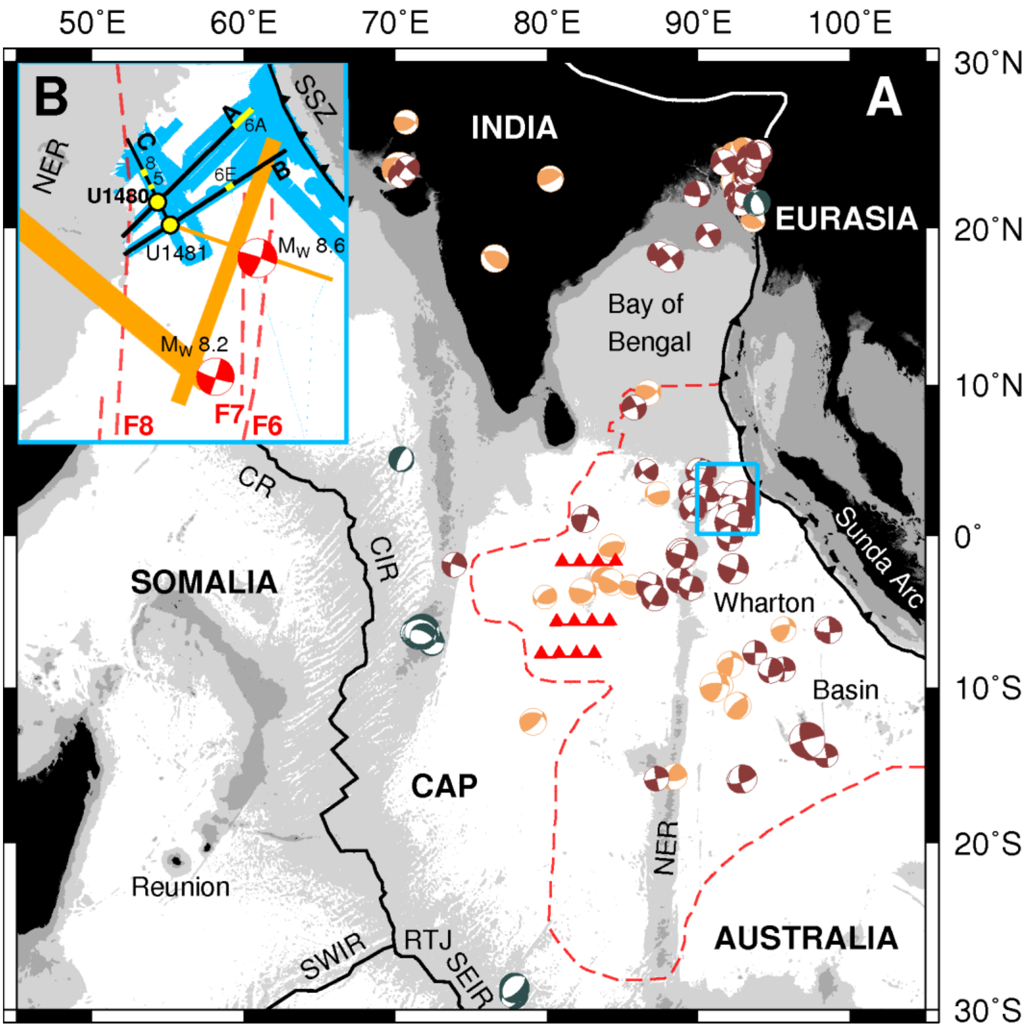

Figure 1. A) Map showing regional tectonic configuration. Red dashed line indicates extent of diffuse deformation (Gordon et al., 1998). Red toothed lines show schematically the area affected by prominent reverse faults (Bull and Scrutton, 1992; Deplus, 2001). Earthquake focal mechanisms within >2 degrees of narrow plate boundaries, scaled based on magnitude: brown=strike-slip; orange=thrust; blue-grey=normal (Gordon and Houseman, 2015, events 5.3 < Mw < 8.6, 1976-2014). Light blue box shows enlarged in part B (and approximate area shown in Fig 10). NER – Ninety East Ridge; CR – Carlsberg Ridge; CIR – Central Indian Ridge; SWIR – South West Indian Ridge; RTJ – Rodriguez Triple Junction; SEIR – South East Indian Ridge; CAP – Capricorn plate. Bathymetry contoured at 2000 m intervals. B).

Yellow dots indicate IODP drill sites. Black lines are multichannel seismic profiles A-C, sections highlighted in yellow indicate the locations of seismic data depicted in Figs. 5, 6 and 8. Light blue shaded area shows multibeam bathymetry coverage used in this study (presented in Fig. 4) Red, dashed lines are fracture zones (Jacob et al., 2014) (nomenclature from Singh et al., 2011). Focal mechanisms for April 2012 events in red, data from Global centroid moment tensor project [www.globalcmt.org]. Orange shaded area shows rupture plane model for 2012 earthquakes from Wei et al., (2013). SSZ – Sumatra Subduction Zone.

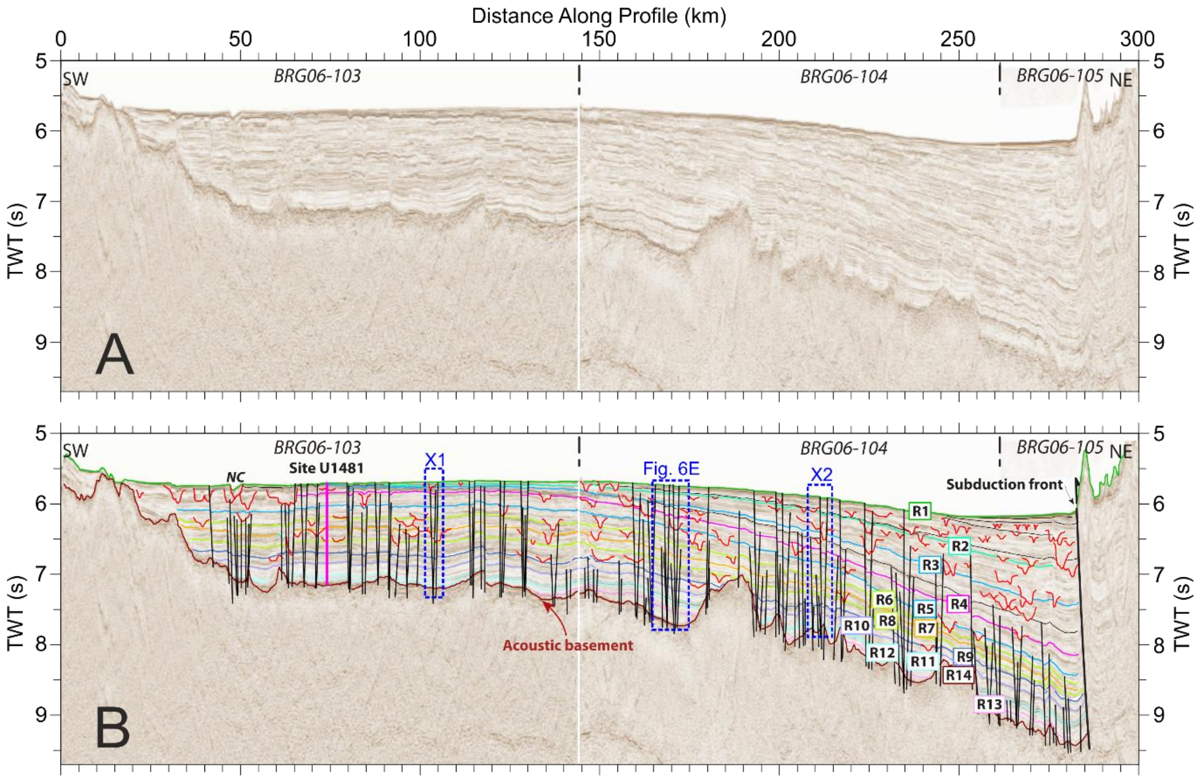

Figure 2. Regional seismic profile B and position of IODP Site U1481 (vertical pink line). (A) Uninterpreted and (B) interpreted, with faults (black), horizons/reflectors (coloured) R1 to R14 and channels (red). Dashed blue boxes indicate the locations of expanded sections (Fig. 6E (see below) and examples X1 and X2 (see supplementary material). NC=Nicobar Channel; NER=Ninety East Ridge. Fig. 9 shows along profile analysis for this profile.

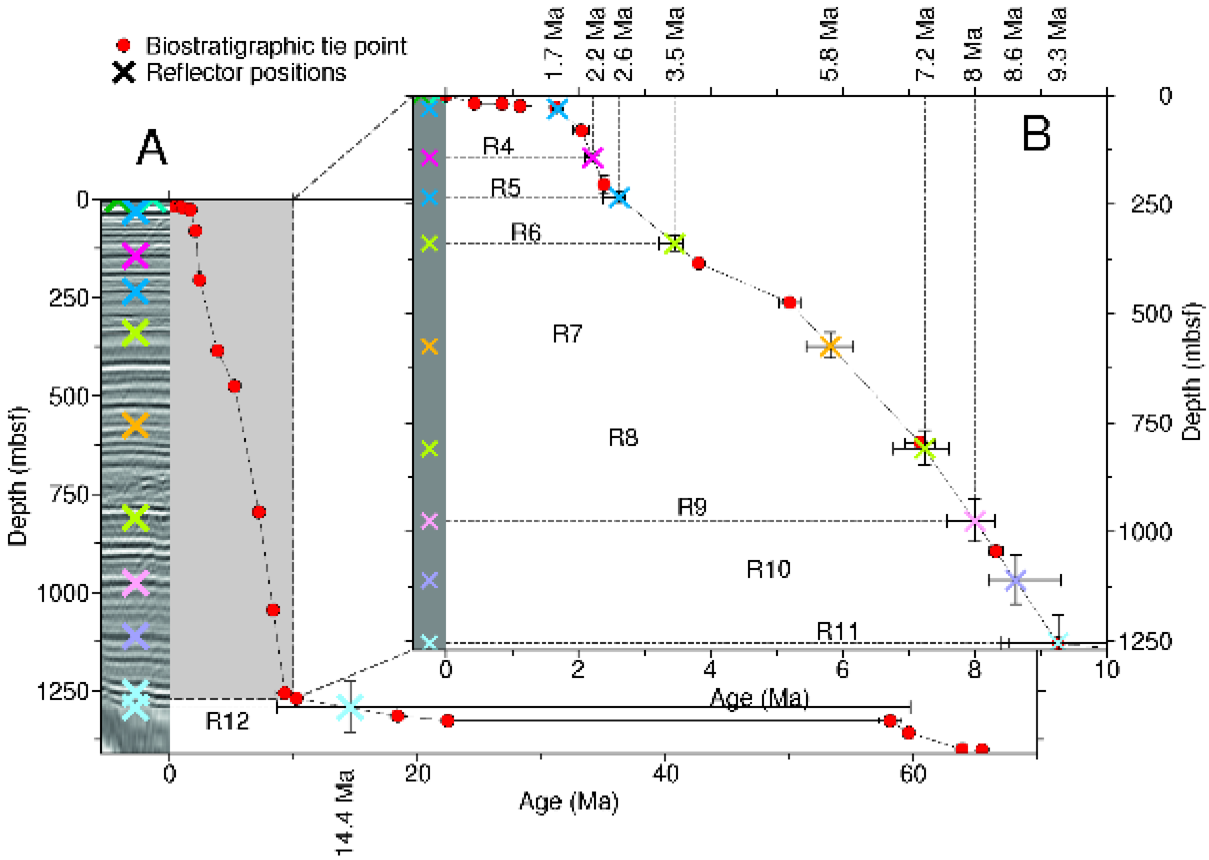

Figure 3. Interpolation of reflector ages from core-seismic integration. Coloured crosses are seismic reflectors (Fig. 2). The age of reflectors is estimated by time-depth conversion and linear sedimentation accumulation rates between biostratigraphic tie points (McNeill et al., 2017a, 2017b). Errors of reflector ages are ±5% due to velocity uncertainty and the age ranges of tie points.

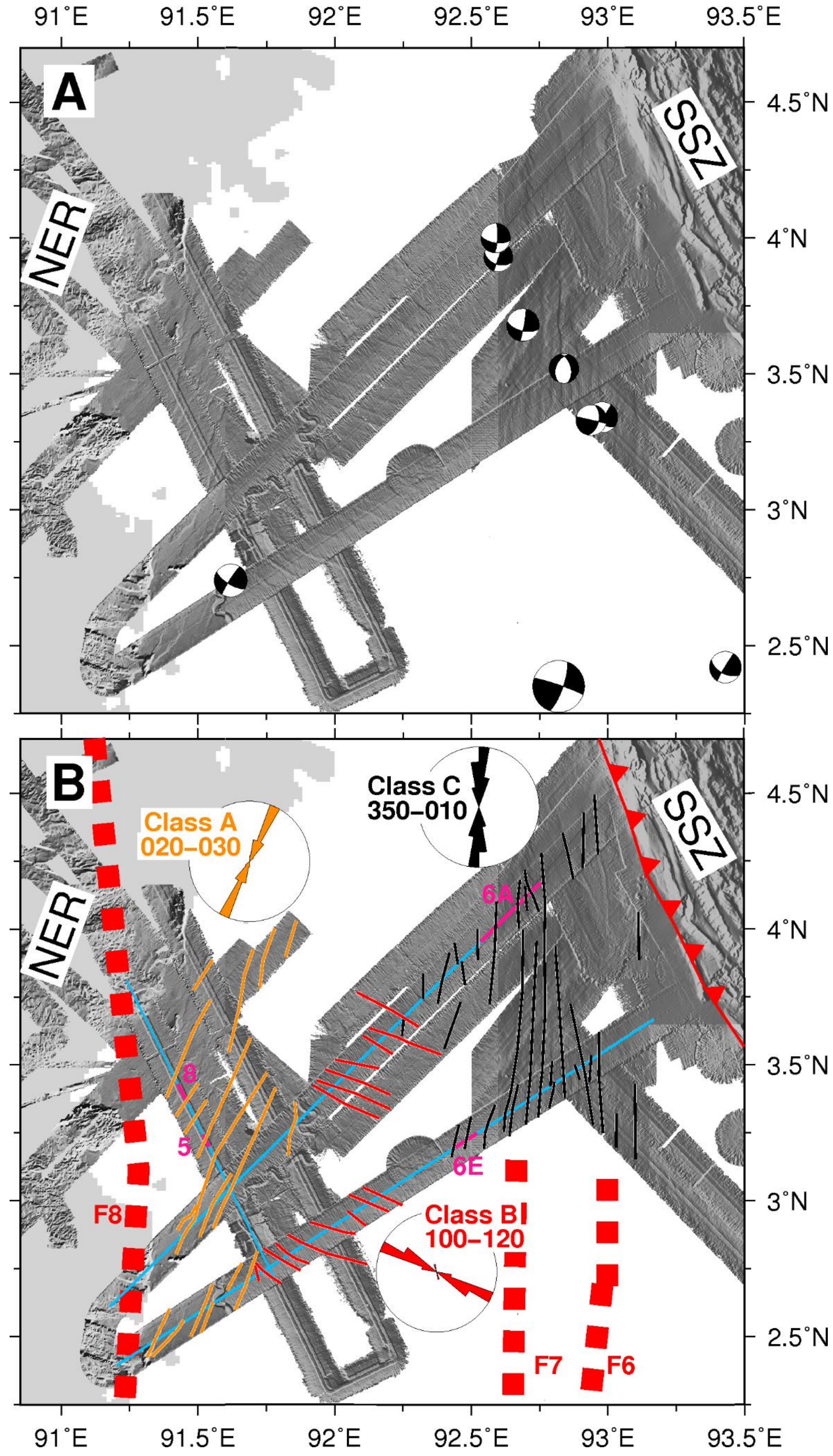

91˚E
91.5˚E
92˚E
92.5˚E
93˚E
93.5˚E
4.5˚N
4˚N
3.5˚N
3˚N
2.5˚N
A
NER
SSZ
B
Class A
020–030
Class C
350–010
Class B
100–120
6A
8
5
6E
F8
F7
F6

740

Figure 4. Distribution of seafloor faulting interpreted from multibeam bathymetry. A) uninterpreted slope map of multibeam data showing intraplate earthquake focal mechanisms (as shown in Fig. 1). B) Interpreted lineations for each fault class (colour coded) and corresponding rose diagrams. Thick red dotted lines represent fracture zones (nomenclature from Singh et al., 2011). Light blue lines indicate seismic profiles and the positions of Figs. 5, 6 and 8 are highlighted in pink.

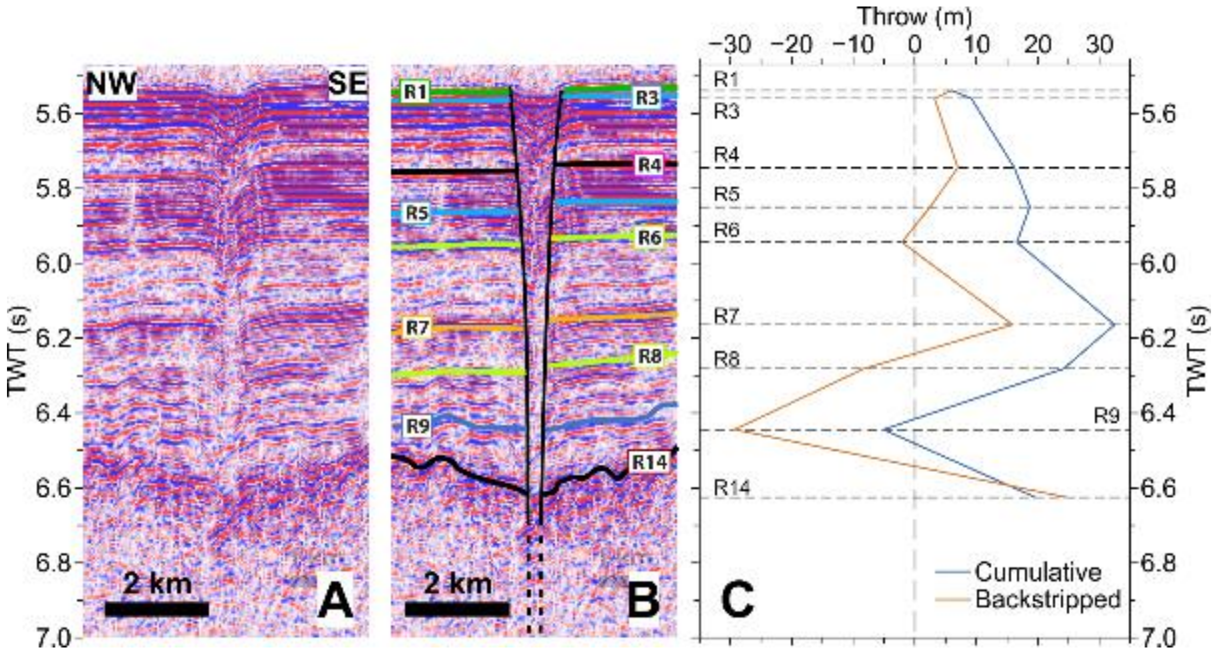

Figure 5. Example Class A fault on NW-SE trending seismic profile C, (A) uninterpreted and (B) interpreted. Note V-shape of reflectors at the position of the fault and apparent layer thickness changes across the fault. (C) displacement analysis of example fault. Cumulative line shows the total net vertical displacement accumulated by each horizon since deposition, backstripped line indicates how vertical displacement has accumulated with time i.e. how much displacement occurred ca the time of deposition of each horizon. Vertical separation attributed positive values for normal and negative for reverse assuming that the footwall is to the SE.

757

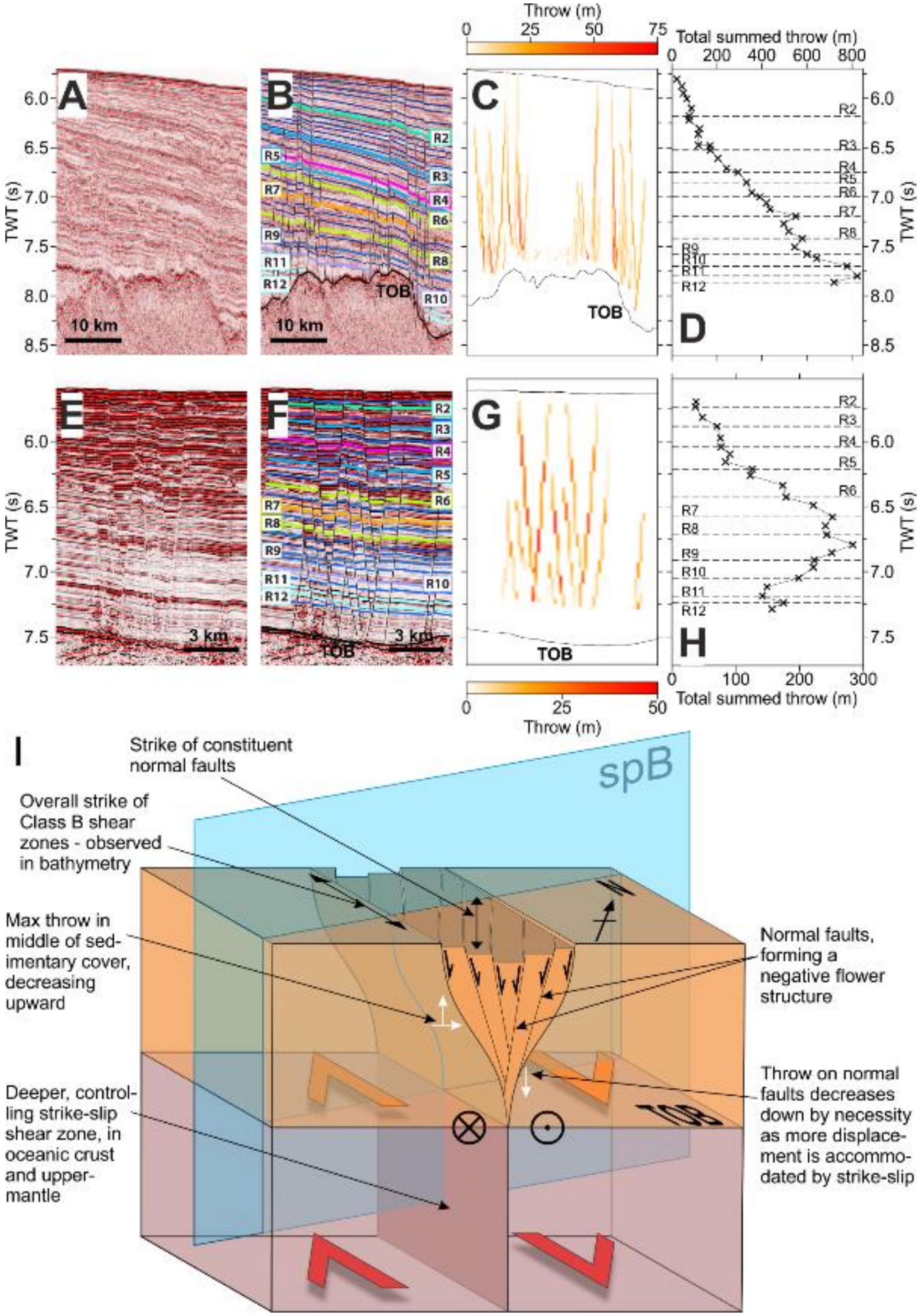

Throw (m)
0 25 50 75
Total summed throw (m)
0 200 400 600 800
A
B
C
D
TWT (s)
TOB
10 km
R2
R3
R4
R5
R6
R7
R8
R9
R10
R11
R12
E
F
G
H
3 km
0 100 200 300
Total summed throw (m)
0 25 50
Throw (m)
I
Strike of constituent normal faults
spB
Overall strike of Class B shear zones - observed in bathymetry
Max throw in middle of sedimentary cover, decreasing upward
Normal faults, forming a negative flower structure
Deeper, controlling strike-slip shear zone, in oceanic crust and upper-mantle
Throw on normal faults decreases down by necessity as more displacement is accommodated by strike-slip
N

Figure 6. A-D Example Class C (fracture zone) faulting. (A) uninterpreted and (B) interpreted seismic sections. Note long-wavelength basement topography. (C) Heat map of fault throw, warmer colours indicate greater amounts of throw (see text for method explanation). (D) Fault throw summed across the whole fault zone against depth in two-way-travel-time (also plotted as example F7N in Fig. 7B). E-H) The same analysis but for Class B faulting. Panel D also plotted as example prof. B in Fig. 7A. In (B and F) subhorizontal coloured lines are used to create plots C and D, and G and H, respectively (where brightly coloured lines are reflectors R1-12, and dull blue lines are additional reflectors interpreted for detailed analysis). TOB – Top of Oceanic Basement. (I) Schematic interpretation of Class B faulting. A purely strike-slip shear fault at depth, within the crust and upper mantle creates extension in the sedimentary cover (see text). spB – Seismic Profile B.

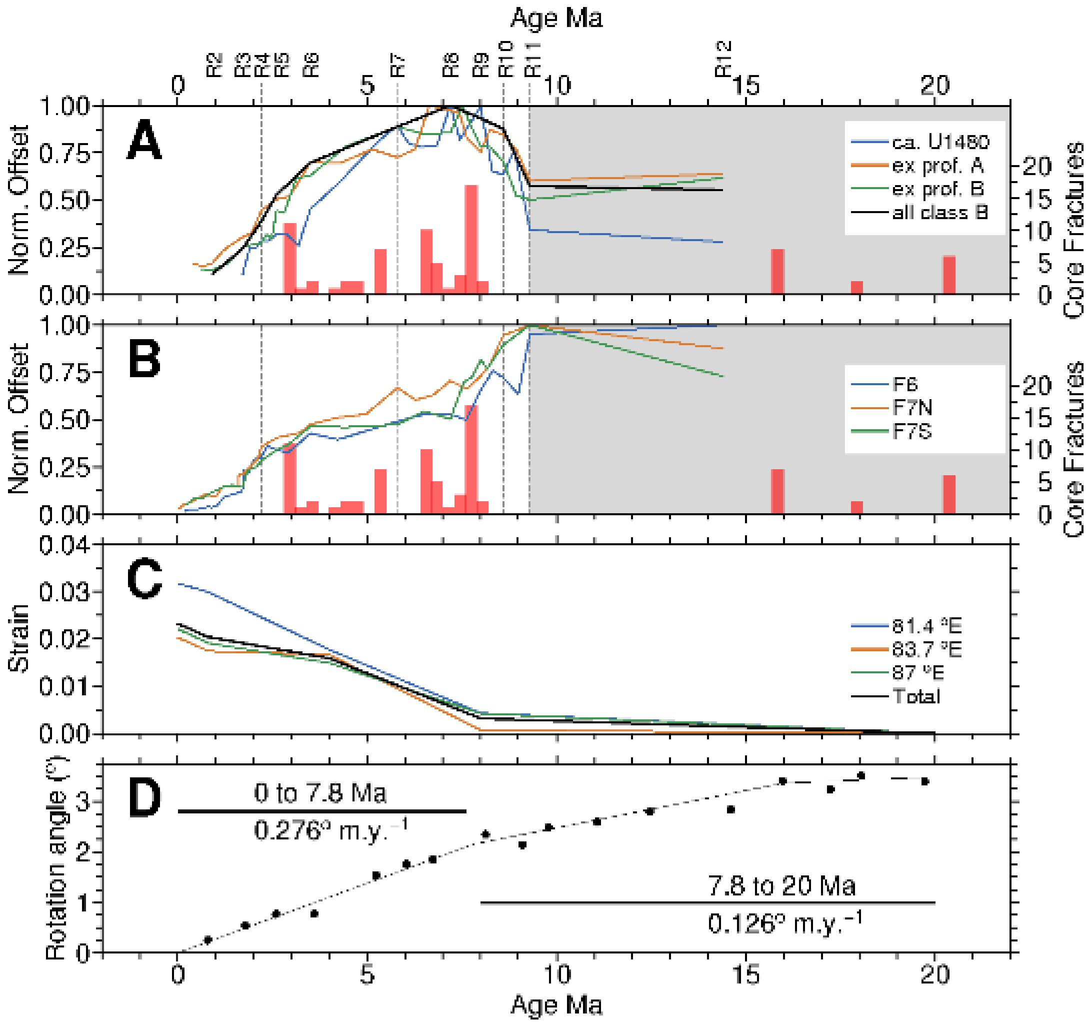

Figure 7. Examples of fault displacement profiles for different fault classes plotted with depth/sediment age alongside strain of faults west of the NER and plate motion history through time. (A) Class B fault displacement with depth/reflector age. Coloured lines are three fault examples; black line is overall average for all Class B faults. (B) Displacement profiles with depth/reflector age for major fracture zones F6 and F7 (the latter from profile A (F7N) and B (F7S). The frequency of fractures detecting in core at site U1480 is adjusted to age and superimposed on both (A) and (B). (C) Analysis by Krishna et al. (2009) for strain budget for faults west of the NER from fault throw, plotted against age. Strain is normalized by deformation extent on each seismic profile used (longitude of N-S profiles indicated). D) India-Capricorn finite rotation angles with time from plate kinematic reconstructions (Bull et

al., 2010), showing acceleration around 8 Ma. Used here as a proxy for India-Australia relative motion.

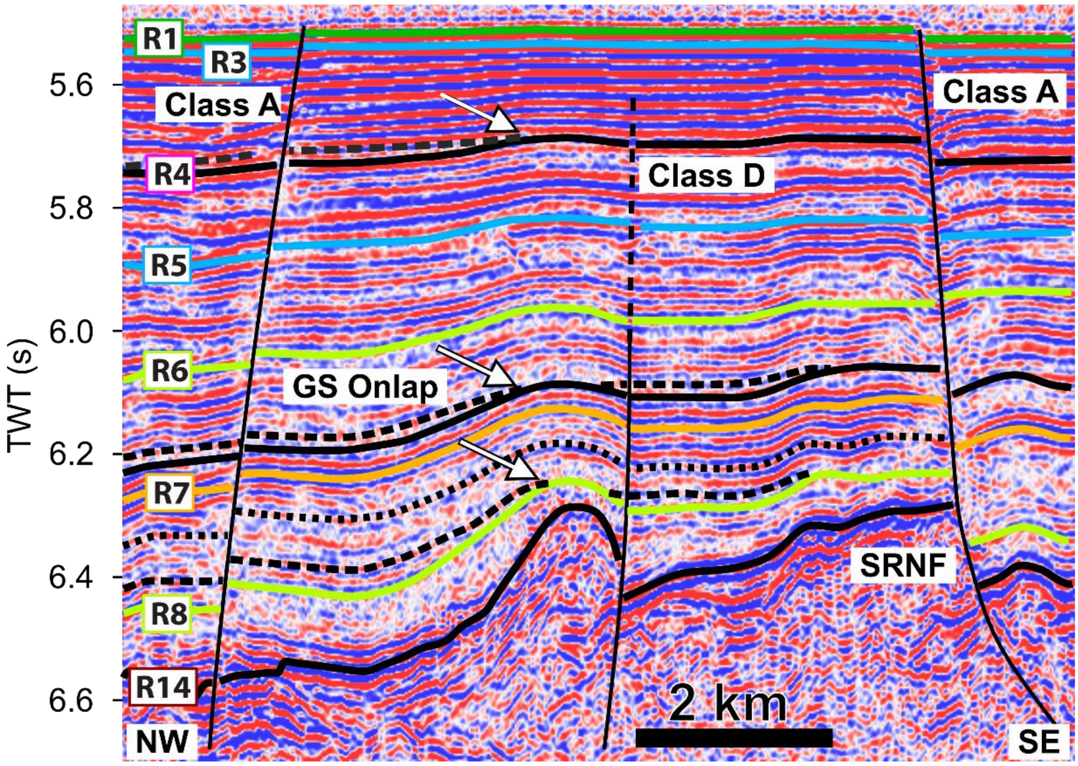

Figure 8. Example Class D reverse fault structure on NW-SE trending profile C. Additional dashed horizons show onlap of growth strata (GS) onto the crest of the fault-propagation fold (indicated by arrows). Also shown is a spreading-ridge-normal-fault (SRNF) that has been re-activated through Class A strike-slip faulting.

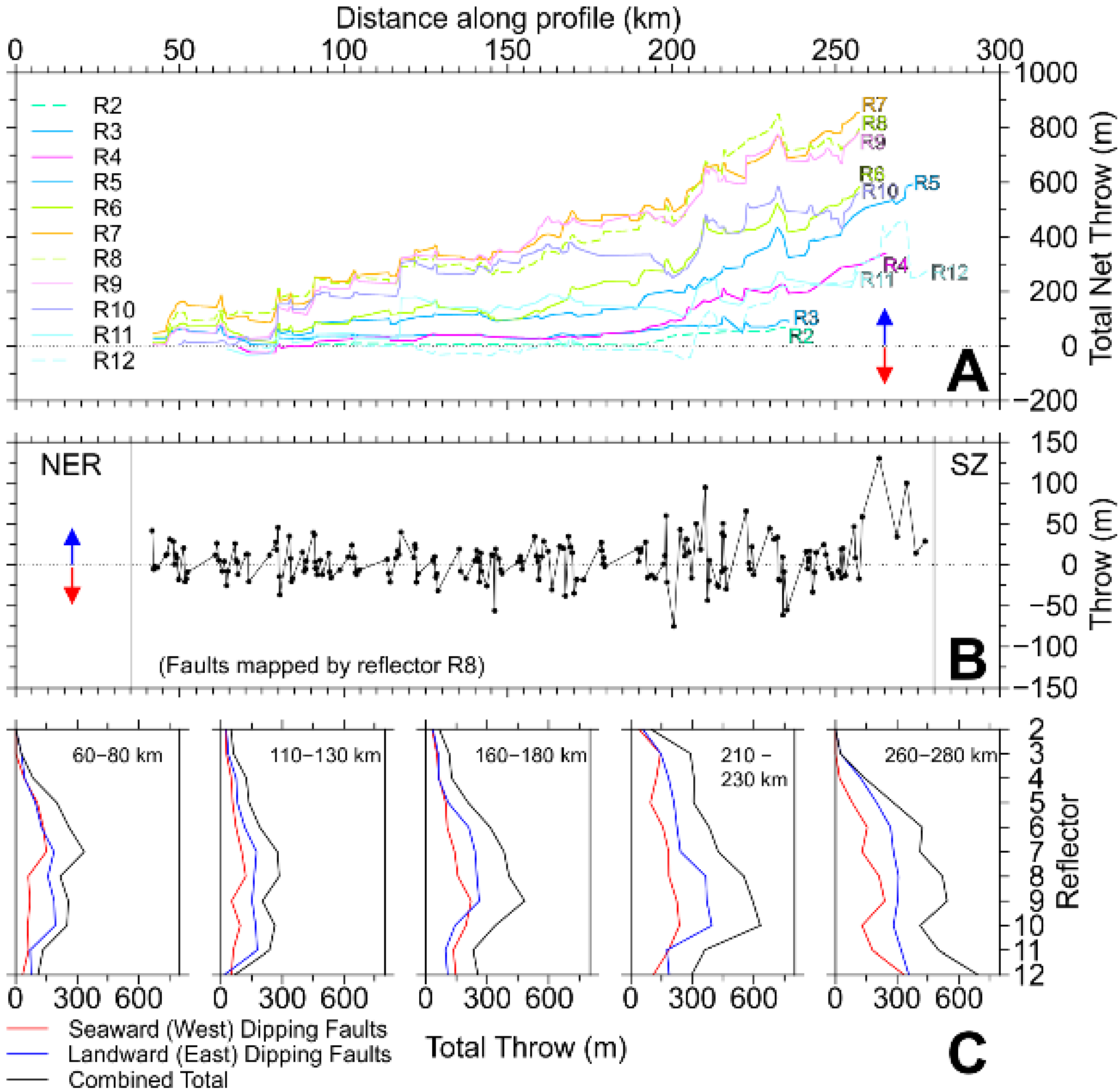

Figure 9. Along-profile B analysis. (A) Differential cumulative throw from west to east for reflector R1-12 as a function of the differential between E- and W-dipping faults, with E-dipping faults assigned positive values (towards the subduction zone) and W-dipping faults assigned negative values (towards the NER), indicating a dominance of E-dipping faults. Red arrow indicates W-dipping faults dominant, blue arrow indicates E-dipping faults dominant. (B). Along profile throw of reflector R8 (~7 Ma) for individual faults (arrows and +ve/-ve values assigned as in (A)). (C) Displacement with depth profiles for a set of example 20 km along-profile segments (from seismic profile B) where throw is summed for all faults within

the segment. Results show changing depth and magnitude of maximum displacement along the profile.

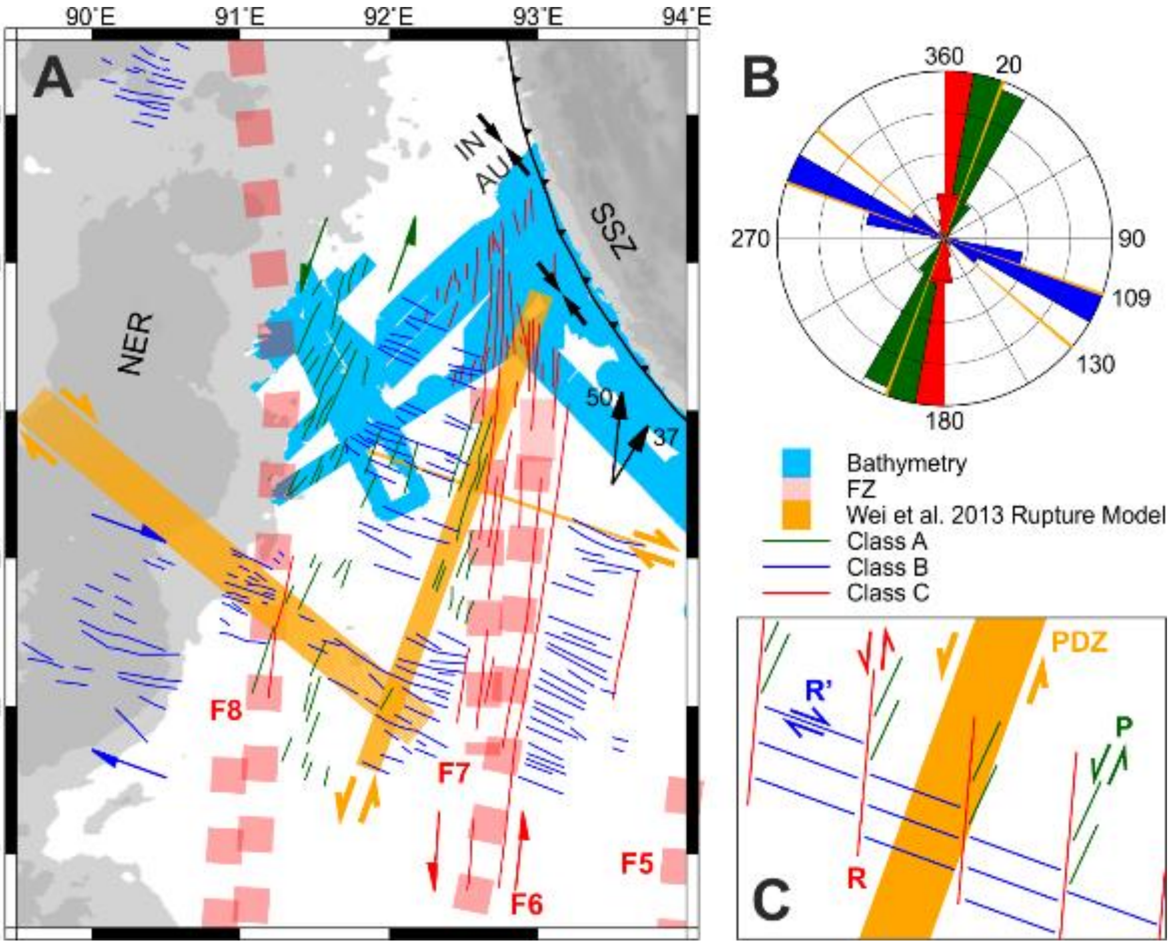

Figure 10. (A) Compiled fault map of the northern Wharton Basin (from this study; Sager et al., 2013; Hananto et al., 2018). Light blue area shows location of bathymetry data used in this study. Pink areas indicate locations of major Wharton Ridge fracture zones (Singh et al., 2011). Orange areas indicate 2012 earthquakes rupture planes (Wei et al., 2013). Faults are: Class A faults and equivalents (green); Class B faults and equivalents (blue); Class C faults and equivalents (red). Green, blue and red arrows indicate sense of displacement on correspondingly coloured faults. Opposing black arrows (IN-AU) indicate principal deviatoric stress (Gordon and Houseman, 2015). Numbered black arrows are plate motion vectors (McNeill and Henstock, 2014) mm/year. (B) Rose diagram showing average fault class orientations and orientations of the rupture planes for the 2012 earthquakes. (C) Schematic of proposed relationship between these fault sets, as Riedel shears forming in

response to a NNE-trending principal displacement zone. NER – Ninety East Ridge, SSZ – Sunda Subduction Zone.